

Parameterized Strain Estimation for Vascular Ultrasound Elastography With Sparse Representation

Hongliang Li, Jonathan Porée^{id}, *Member, IEEE*, Boris Chayer, Marie-Hélène Roy Cardinal^{id}, and Guy Cloutier^{id}, *Senior Member, IEEE*

Abstract—Ultrasound vascular strain imaging has shown its potential to interrogate the motion of the vessel wall induced by the cardiac pulsation for predicting plaque instability. In this study, a sparse model strain estimator (SMSE) is proposed to reconstruct a dense strain field at a high resolution, with no spatial derivatives, and a high computation efficiency. This sparse model utilizes the highly-compacted property of discrete cosine transform (DCT) coefficients, thereby allowing to parameterize displacement and strain fields with truncated DCT coefficients. The derivation of affine strain components (axial and lateral strains and shears) was reformulated into solving truncated DCT coefficients and then reconstructed with them. Moreover, an analytical solution was derived to reduce estimation time. With simulations, the SMSE reduced estimation errors by up to 50% compared with the state-of-the-art window-based Lagrangian speckle model estimator (LSME). The SMSE was also proven to be more robust than the LSME against global and local noise. For *in vitro* and *in vivo* tests, residual strains assessing cumulated errors with the SMSE were 2 to 3 times lower

than with the LSME. Regarding computation efficiency, the processing time of the SMSE was reduced by 4 to 25 times compared with the LSME, according to simulations, *in vitro* and *in vivo* results. Finally, phantom studies demonstrated the enhanced spatial resolution of the proposed SMSE algorithm against LSME.

Index Terms—Affine-based model strain, discrete cosine transform, high temporal and spatial resolutions, optical flow, sparse representation, ultrasound elastography, principal strains.

I. INTRODUCTION

VASCULAR ultrasound strain imaging has shown its potential to extract the motion of the vessel wall caused by the cardiac pulsation for the purpose of trying predicting carotid artery plaque instability [1]. Currently, window-based methods are widely used to estimate two-dimensional (2-D) strain maps from radiofrequency (RF) datasets, using either image amplitude [2]–[6] or phase information [7]–[10]. Specifically, pre- and post-motion images are divided into overlapping windows. Assuming that motions of pixels within a window are the same, window-based methods locally derive mean displacements and/or strains within that window. However, there is a trade-off among window parameters, quality of a strain image and computation efficiency. A small window size with a large overlap are desired for a better resolution at the cost of a high computational load. A large overlap nevertheless introduces worm artifact filtering [11], [12]. On the other hand, a small window size results in larger estimation variances.

An alternative way is to globally estimate pixel-wise motions in a region of interest (ROI) instead of using overlapping windows. To our knowledge, no pixel-based algorithms were proposed for vascular ultrasound elastography. Some approaches have been developed for quasi-static elastography [13]–[18], Doppler vector flow [19], myocardial motion tracking [20], [21] and computer vision [22]. Usually, one formulates pixel-based motion estimations as an optimization problem, where a cost function incorporating a data term and a regularization term is minimized. Sparse representations of motion fields were also introduced into motion estimators [23]–[25], where dense motions can be recovered using the compressed sensing theory [26] with a small portion of all samples. However, these models only consider displacement or velocity fields. Additional

Manuscript received May 21, 2020; accepted June 17, 2020. Date of publication June 25, 2020; date of current version November 30, 2020. This work was supported in part by the Collaborative Health Research Program of the Natural Sciences and Engineering Research Council of Canada under Grant CHRP-462240-2014 and in part by the Canadian Institutes of Health Research under Grant CPG-134748. The work of Hongliang Li was supported by the Québec Bioimaging Network of the Fonds de Recherche Québec Santé (Institute of Biomedical Engineering, University of Montréal). (*Corresponding author: Guy Cloutier.*)

Hongliang Li is with the Laboratory of Biorheology and Medical Ultrasonics, University of Montreal Hospital Research Center (CRCHUM), Montreal, QC H2X 0A9, Canada, and also with the Institute of Biomedical Engineering, University of Montreal, Montreal, QC H3T 1J4, Canada (e-mail: hongliang.li@umontreal.ca).

Jonathan Porée was with the Laboratory of Biorheology and Medical Ultrasonics, University of Montreal Hospital Research Center (CRCHUM), Montreal, QC H2X 0A9, Canada. He is now with the École Polytechnique of Montreal, Montreal, QC H3T 1J4, Canada (e-mail: jonathan.poree@gmail.com).

Boris Chayer and Marie-Hélène Roy Cardinal are with the Laboratory of Biorheology and Medical Ultrasonics, University of Montreal Hospital Research Center (CRCHUM), Montreal, QC H2X 0A9, Canada (e-mail: boris.chayer@crchum.qc.ca; marie-helene.roy-cardinal@polymtl.ca).

Guy Cloutier is with the Laboratory of Biorheology and Medical Ultrasonics, University of Montreal Hospital Research Center (CRCHUM), Montreal, QC H2X 0A9, Canada, also with the Institute of Biomedical Engineering, University of Montreal, Montreal, QC H3T 1J4, Canada, and also with the Department of Radiology, Radio-Oncology and Nuclear Medicine, University of Montreal, Montreal, QC H3T 1J4, Canada (e-mail: guy.cloutier@umontreal.ca).

This article has supplementary material provided by the authors and color versions of one or more figures available at <https://doi.org/10.1109/TMI.2020.3005017>.

Digital Object Identifier 10.1109/TMI.2020.3005017

gradient operations on displacement fields are required when strain fields are imperative. To reduce estimation variance, a least-squares strain estimator (LSQSE) [27] or a low-pass digital differentiator [28] is commonly used to determine derivatives of displacement fields by considering multiple points instead of two points. However, there is a trade-off between variance, strain contrast and resolution [27], [28].

Affine model-based estimation could circumvent the limitation of derivative operations but remains into the category of window-based methods [6], [10], [29]. An optical-flow-based Lagrangian speckle model estimator (LSME) including an incompressibility constraint was proposed to obtain robust strain estimates in the context of vascular elastography [6]. A performance evaluation of the LSME and of an affine phase-based estimator (APBE) was also conducted showing the superiority of the LSME [10]. Although some of aforementioned pixel-based methods [13], [16] have considered axial or lateral strain estimations, shear strains are still not assessed. To our knowledge, a pixel-wise vascular strain estimator with an affine model considering all strain components without spatial derivatives on displacements has not yet been proposed.

Computation efficiency is another issue that needs to be addressed. Computation time of window-based methods depends on the window size and on the level of overlap. Specifically, the computation time of a whole motion field corresponds to the sum of the time required to locally perform successive window computations. To reduce the computation load, all pixels inside a ROI can be used to solve the dense motion field globally. However, this usually requires to optimize iteratively a cost function until convergence, which also impacts computation time. Rivaz's group proposed to convert the optimization problem into solving a sparse linear system of equations using a computationally efficient iterative algorithm [17]. However, the proposed method is still based on displacement estimates. Recently, an effort was made to change the iterative optimization into a least squares scheme to obtain analytic solutions of vector Doppler flow maps [30]. This strategy was adapted here for vascular strain imaging.

In this study, we propose to parameterize strain fields using a sparse representation based on discrete cosine transform (DCT) coefficients, allowing to directly derive strains without explicit gradient operations. This parameterized implementation also enables strains to be solved analytically using a least squares scheme. The proposed vascular sparse model-based strain estimator (SMSE) is providing high-resolution pixel-wise affine strain estimates with high accuracy and high computation efficiency compared with the LSME implementation.

II. ALGORITHM DESCRIPTION

The proposed algorithm is within the framework of the Horn-Schunck (HS) optical flow method. Unlike HS that only considers a smoothness constraint, a nearly incompressibility regularization term was also introduced into the cost function to improve lateral strain estimation. Moreover, motion fields were parameterized with a truncated discrete cosine basis. This sparse representation was formulated to solve strain

fields using a least squares method instead of an optimization problem, as in the HS algorithm. The pixel-based solution is providing axial, lateral and shear strain components simultaneously.

A. Cost Function With Smoothness and Nearly Incompressibility Constraints

1) *Data Term*: The cost function consists of data and regularization terms. The data term is from the optical flow constraint equation, which implies that the intensity between two consecutive images is not changing,

$$I_x U_x + I_y U_y + I_t = 0, \quad (1)$$

where I_x , I_y are the spatial gradient of the image intensity, I_t denotes the temporal gradient of the image intensity, and U_x , U_y are the unknown lateral and axial displacements. Spatial and temporal gradient operations on the image intensity in the optical flow method can induce variance due to the discontinuity of the image intensity. One can apply a low-pass filter on the image prior to the optical flow estimation to reduce variance but at the expense of the bias. In this study, we did not use any filtering operations but simply the central difference to obtain image gradients. In Eq. (1), there are two unknown variables. Therefore, additional constraints need to be added to overcome the ill-posed problem.

2) *Smoothness Constraint*: Horn and Schunck proposed a classical first-order optical flow smoothness constraint [22]. It assumes the object undergoes rigid motions to minimize the square magnitude of the gradient displacement field $\vec{U} = (U_x, U_y)$, namely $(\frac{\partial U_x}{\partial x})^2 + (\frac{\partial U_x}{\partial y})^2 + (\frac{\partial U_y}{\partial x})^2 + (\frac{\partial U_y}{\partial y})^2$. However, the motion of a fluid flow also exhibits divergence and vorticity. In [31], a second-order divergence-curl smoothness was used to allow for a more physically meaningful smoothness regularization for fluid-like conditions. Likewise, motions in biological tissues are complex and include not only translations, but also rotations and non-rigid deformations (compression or expansion). Thus, the curl-related rotation, and divergence-related compression (expansion) should be regularized. In [32], [33], the second-order smoothness constraint was generalized and decomposed into the first-order derivative of divergence and curl of the optical flow field as $\alpha \|\nabla \text{div} \vec{U}\|^2 + \beta \|\nabla \text{curl} \vec{U}\|^2$, where $\text{div} \vec{U} = \frac{\partial U_x}{\partial x} + \frac{\partial U_y}{\partial y}$, $\text{curl} \vec{U} = -\frac{\partial U_x}{\partial y} + \frac{\partial U_y}{\partial x}$, $\nabla(\bullet)$ represents the sum of the gradients of components, and $\|\bullet\|^2$ is the L2 norm. When $\alpha = \beta$, this constraint is equivalent to the second-order smoothness given by: $(\frac{\partial^2 U_x}{\partial x^2})^2 + (\frac{\partial^2 U_x}{\partial y^2})^2 + (\frac{\partial^2 U_x}{\partial x \partial y})^2 + (\frac{\partial^2 U_x}{\partial y \partial x})^2 + (\frac{\partial^2 U_y}{\partial x^2})^2 + (\frac{\partial^2 U_y}{\partial y^2})^2 + (\frac{\partial^2 U_y}{\partial x \partial y})^2 + (\frac{\partial^2 U_y}{\partial y \partial x})^2$. The advantage of this second order smoothness constraint is that it favors the smoothness of the divergence and curl of the flow field. In fact, the divergence and curl quantify the flow compression and rotation, respectively, which are dominant in flow motion representations of biological tissues. Here, we incorporated this second-order smoothness constraint that is tailored towards complex flow fields [34], [35] into the cost function. Thus, the regularized cost function including the data term of Eq. (1) and the

second-order smoothness constraint is defined as:

$$\min_{U_x, U_y} \left\{ (I_x U_x + I_y U_y + I_t)^2 + \lambda_s \left(\left(\frac{\partial^2 U_x}{\partial x^2} \right)^2 + \left(\frac{\partial^2 U_x}{\partial y^2} \right)^2 + \left(\frac{\partial^2 U_x}{\partial x \partial y} \right)^2 + \left(\frac{\partial^2 U_x}{\partial y \partial x} \right)^2 + \left(\frac{\partial^2 U_y}{\partial x^2} \right)^2 + \left(\frac{\partial^2 U_y}{\partial y^2} \right)^2 + \left(\frac{\partial^2 U_y}{\partial x \partial y} \right)^2 + \left(\frac{\partial^2 U_y}{\partial y \partial x} \right)^2 \right\}, \quad (2)$$

where λ_s is a regularization parameter to control the influence of the smoothness constraint.

3) Nearly Incompressibility Constraint: No volume change is experienced in incompressible materials under small deformations. Some biological tissues can be considered as nearly incompressible [34]; this is the case of human arteries [36]. In the field of ultrasound strain imaging, arterial tissue incompressibility was used to improve the quality of strain estimations [6], [10], [37]. Assuming 2-D plane strain, a null divergence of the displacement field \vec{U} is considered, *i.e.* $\text{div} \vec{U} = \frac{\partial U_x}{\partial x} + \frac{\partial U_y}{\partial y} = 0$. Upon this assumption, the lateral strain is constrained to be the negative of the axial strain, as used in [6]. In the current study, we integrated instead this incompressibility constraint into Eq. (3) to obtain an additional regularization term to constrain the divergence close to zero:

$$\min_{U_x, U_y} \left\{ (I_x U_x + I_y U_y + I_t)^2 + \lambda_s \left(\left(\frac{\partial^2 U_x}{\partial x^2} \right)^2 + \left(\frac{\partial^2 U_x}{\partial y^2} \right)^2 + \left(\frac{\partial^2 U_x}{\partial x \partial y} \right)^2 + \left(\frac{\partial^2 U_x}{\partial y \partial x} \right)^2 + \left(\frac{\partial^2 U_y}{\partial x^2} \right)^2 + \left(\frac{\partial^2 U_y}{\partial y^2} \right)^2 + \left(\frac{\partial^2 U_y}{\partial x \partial y} \right)^2 + \left(\frac{\partial^2 U_y}{\partial y \partial x} \right)^2 \right) + \lambda_d \left(\frac{\partial U_x}{\partial x} + \frac{\partial U_y}{\partial y} \right)^2 \right\}, \quad (3)$$

where λ_d is a regularization parameter to modulate the influence of the incompressibility constraint. Contrary to the implementation of [6], this regularization term does not impose tissue incompressibility, but constrains it into the cost function to obtain a nearly incompressible condition. This soft constraint avoids an ill-conditioned problem when forcing the divergence to zero. A similar quasi incompressibility constraint was utilized for the registration of magnetic resonance (MR) tissue images [34], [38], and for Doppler flow and tissue Doppler mapping [30], [39], [40]. It is used for the first time into the framework of an optical-flow-based non-invasive vascular elastography method.

To find suitable displacement fields minimizing Eq. (2), one can solve Euler-Lagrange equations, which is a typical variational problem. A detailed solution description can be found in [22]. In the current study, displacement fields were parameterized with a truncated discrete cosine basis (see Section II-B). The minimization problem was rewritten as a linear least squares problem.

B. Sparse Representation and Reconstruction of the Strain Field

1) Discrete Cosine Representation: In this study, the displacement field used in the minimization of Eq. (3)

was expressed with type-II discrete cosine basis functions written as:

$$U_x(x, y) = \sum_m^{M_t} \sum_n^{N_t} c_{m,n}^x \cos(k_x^m(2x+1)) \cos(k_y^n(2y+1))$$

$$U_y(x, y) = \sum_m^{M_t} \sum_n^{N_t} c_{m,n}^y \cos(k_x^m(2x+1)) \cos(k_y^n(2y+1)), \quad (4)$$

where $k_x^m = \frac{m}{2M}\pi$, $k_y^n = \frac{n}{2N}\pi$, with the grid size (M, N) in lateral and axial directions, and (M_t, N_t) being the size of the truncated discrete cosine basis (*i.e.*, $M_t \leq M$, $N_t \leq N$). Section III-E justifies the choice of M_t and N_t . In Eq. (4), $c_{m,n}^x$ and $c_{m,n}^y$ are the DCT coefficients of the lateral and axial displacement components. In [23], it was verified that the representation of an optical flow vector is sparse in wavelet or DCT domains. The motivation for using DCT is its property of energy compaction [41], which allows to reconstruct images from a small number of DCT coefficients instead of all coefficients of dimensions (M, N) (see an example of a DCT frequency decomposition of a principal minor strain map in Fig. S1 of supplementary materials). Thus, this property of the DCT sparse representation enables improving the computation efficiency for reconstructing motion fields by using only DCT coefficients with significant magnitudes.

Once the motion field is represented by sparse basis functions, the motion estimation problem becomes an optimization problem regarding the coefficients. In [24] and [25], the optical flow field was encoded into sparse representation and recovered from much fewer pixels using the compressed sensing theory by imposing a sparsity constraint on coefficients. In the next section, we propose an alternative by using truncated DCT coefficients with which the solution to the optimization problem in Eq. (3) can be derived in a direct way instead of an iterative process.

Another advantage of parameterized representations of motion fields is that strain fields can be represented by DCT basis transformations, which avoid to explicitly compute derivative of noisy estimated displacements. Specifically, once DCT coefficients are resolved, strain components are represented by a combination of estimated DCT coefficients and DCT basis transformations, as shown here:

$$S_{xx} = \frac{\partial U_x}{\partial x} = \sum_m^{M_t} \sum_n^{N_t} c_{m,n}^x (-2k_x^m) \sin(k_x^m(2x+1)) \times \cos(k_y^n(2y+1))$$

$$S_{xy} = \frac{\partial U_x}{\partial y} = \sum_m^{M_t} \sum_n^{N_t} c_{m,n}^x (-2k_y^n) \cos(k_x^m(2x+1)) \times \sin(k_y^n(2y+1))$$

$$S_{yy} = \frac{\partial U_y}{\partial y} = \sum_m^{M_t} \sum_n^{N_t} c_{m,n}^y (-2k_y^n) \cos(k_x^m(2x+1)) \times \sin(k_y^n(2y+1))$$

$$S_{yx} = \frac{\partial U_y}{\partial x} = \sum_m^{M_t} \sum_n^{N_t} c_{m,n}^y (-2k_x^m) \sin(k_x^m(2x+1)) \times \cos(k_y^n(2y+1)), \quad (5)$$

where S_{xx} , S_{xy} , S_{yy} , S_{yx} are lateral strain, lateral shear, axial strain and axial shear, respectively. Cartesian strain components were combined and represented as principal minor and major strain tensors, ε_{min} , ε_{max} , where:

$$\varepsilon_{min,max} = \frac{S_{xx} + S_{yy}}{2} \pm \sqrt{\left(\frac{S_{xx} - S_{yy}}{2}\right)^2 + \left(\frac{S_{xy} + S_{yx}}{2}\right)^2}. \quad (6)$$

2) Regularized Weighted Least Squares Estimation: The proposed algorithm is capable of reconstructing dense displacement and strain fields at each pixel of an image of size $M \times N$. A strain field of a down-sampled image can also be computed with less computational complexity. Since the displacement field was parameterized with the discrete cosine basis, the cost function in Eq. (3) should be expressed in terms of DCT coefficients and the minimization problem formulated as a solution of a system of linear equations, as explained below.

Let $\mathbf{c} = [\mathbf{c}_x^T, \mathbf{c}_y^T]^T$ be a column vector with length $2M_t N_t$, where $\mathbf{c}_x = [\dots, c_{m,n}^x, \dots]^T$ and $\mathbf{c}_y = [\dots, c_{m,n}^y, \dots]^T$ are the DCT coefficients of lateral and axial displacement fields, respectively. To parameterize the cost function in terms of \mathbf{c} , all pixels in the ROI are considered and then the data term, and smoothness and nearly incompressibility constraints, are represented in matrix form, respectively. Let $\mathbf{U} = [\mathbf{U}_x^T, \mathbf{U}_y^T]^T$ represent the displacement field, where $\mathbf{U}_x = [\dots, U_x, \dots]^T$ and $\mathbf{U}_y = [\dots, U_y, \dots]^T$ are column vectors of lateral and axial displacements with lengths MN , respectively. By defining \mathbf{B} as a discrete cosine transform matrix with size $MN \times M_t N_t$, and $\{\mathbf{B}\}_{i,M_t n+m} = \cos(k_x^m(2x_i + 1)) \cos(k_y^n(2y_i + 1))$, where i indicates the pixel index, the displacement fields as shown in Eq. (4) can be expressed in matrix form as $\mathbf{U}_x = \mathbf{B}\mathbf{c}_x$ and $\mathbf{U}_y = \mathbf{B}\mathbf{c}_y$.

Let $\{\mathbf{I}_{of,x}\}_{i,i} = I_x(x_i, y_i)$, $\{\mathbf{I}_{of,y}\}_{i,i} = I_y(x_i, y_i)$, and $\{\mathbf{I}_{of,t}\}_{i,i} = -I_t(x_i, y_i)$ be diagonal matrices with size $MN \times MN$ containing image gradients of all pixels, where the subscript “of” stands for optical flow. Considering abovementioned displacements \mathbf{U}_x and \mathbf{U}_y , the data term as shown in Eq. (1) is then written as $\mathbf{I}_{of,x}\mathbf{B}\mathbf{c}_x + \mathbf{I}_{of,y}\mathbf{B}\mathbf{c}_y - \mathbf{I}_{of,t}$, which can be represented in matrix form as:

$$\mathbf{D}_{of}\mathbf{B}_{of}\mathbf{c} - \mathbf{I}_{of,t}, \quad (7)$$

where $\mathbf{D}_{of} = [\mathbf{I}_{of,x} \ \mathbf{I}_{of,y}]$ with size $MN \times 2MN$, and $\mathbf{B}_{of} = \begin{bmatrix} \mathbf{B} & \mathbf{0} \\ \mathbf{0} & \mathbf{B} \end{bmatrix}$.

The cost function of Eq. (3) introduced a nearly incompressibility constraint to govern a 2-D divergence-free displacement field. Since the displacement field \mathbf{U} is expressed as $\mathbf{U}_x = \mathbf{B}\mathbf{c}_x$ and $\mathbf{U}_y = \mathbf{B}\mathbf{c}_y$, the divergence of \mathbf{U} can be represented by a combination of first-order derivative transformations of \mathbf{B} and \mathbf{c} . Specifically, let $\mathbf{B}^x = \dot{D}_x\mathbf{B}$ and $\mathbf{B}^y = \dot{D}_y\mathbf{B}$ be first-order derivatives of \mathbf{B} in lateral and axial directions, respectively, where \dot{D} stands for the first-order derivative operator. Thus, the nearly incompressibility constraint, $\frac{\partial U_x}{\partial x} + \frac{\partial U_y}{\partial y}$, is presented as $\dot{D}_x\mathbf{B}\mathbf{c}_x + \dot{D}_y\mathbf{B}\mathbf{c}_y$ when considering the full

displacement field. Using $\mathbf{B}^x = \dot{D}_x\mathbf{B}$ and $\mathbf{B}^y = \dot{D}_y\mathbf{B}$, the nearly incompressibility constraint becomes

$$\mathbf{B}_d\mathbf{c}, \quad (8)$$

where $\mathbf{B}_d = [\mathbf{B}^x \ \mathbf{B}^y]$.

Likewise, the second-order smoothness constraint, $\left(\frac{\partial^2 U_x}{\partial x^2}\right)^2 + \left(\frac{\partial^2 U_x}{\partial y^2}\right)^2 + \left(\frac{\partial^2 U_x}{\partial x \partial y}\right)^2 + \left(\frac{\partial^2 U_x}{\partial y \partial x}\right)^2 + \left(\frac{\partial^2 U_y}{\partial x^2}\right)^2 + \left(\frac{\partial^2 U_y}{\partial y^2}\right)^2 + \left(\frac{\partial^2 U_y}{\partial x \partial y}\right)^2 + \left(\frac{\partial^2 U_y}{\partial y \partial x}\right)^2$, can also be represented as a linear combination of second-order derivative transformations of \mathbf{B} and \mathbf{c} . Specifically, the second-order smoothness constraint in terms of displacement fields, $\mathbf{U}_x = \mathbf{B}\mathbf{c}_x$ and $\mathbf{U}_y = \mathbf{B}\mathbf{c}_y$, can be represented as $\ddot{D}_{xx}\mathbf{B}\mathbf{c}_x + \ddot{D}_{yy}\mathbf{B}\mathbf{c}_x + \ddot{D}_{xy}\mathbf{B}\mathbf{c}_x + \ddot{D}_{yx}\mathbf{B}\mathbf{c}_x + \ddot{D}_{xx}\mathbf{B}\mathbf{c}_y + \ddot{D}_{yy}\mathbf{B}\mathbf{c}_y + \ddot{D}_{xy}\mathbf{B}\mathbf{c}_y + \ddot{D}_{yx}\mathbf{B}\mathbf{c}_y$ in terms of \mathbf{B} and \mathbf{c} . Let $\mathbf{B}^* = \ddot{D}_{xx}\mathbf{B} + \ddot{D}_{yy}\mathbf{B} + \ddot{D}_{xy}\mathbf{B} + \ddot{D}_{yx}\mathbf{B}$, where \ddot{D} stands for the second-order derivative operator applied on pixel coordinates. Thus, the second-order smoothness constraint is:

$$\mathbf{B}_s\mathbf{c}, \quad (9)$$

where $\mathbf{B}_s = [\mathbf{B}^* \ \mathbf{B}^*]$.

By introducing above matrix representations of the data term, nearly incompressibility term and smoothness term into the cost function (Eq. (3)), the minimization problem can be rewritten as:

$$\min_{\mathbf{c}} \left\{ (\mathbf{D}_{of}\mathbf{B}_{of}\mathbf{c} - \mathbf{I}_{of,t})^T (\mathbf{D}_{of}\mathbf{B}_{of}\mathbf{c} - \mathbf{I}_{of,t}) + \lambda_s (\mathbf{B}_s\mathbf{c})^T (\mathbf{B}_s\mathbf{c}) + \lambda_d (\mathbf{B}_d\mathbf{c})^T (\mathbf{B}_d\mathbf{c}) \right\}, \quad (10)$$

where T denotes the matrix transposition. To get the solution \mathbf{c} , we can combine terms using the distributive property of the cost function after straightforward matrix calculations, and let its partial derivative regarding \mathbf{c} be equal to zero. Then, the minimization problem is reformulated into a linear system:

$$\mathbf{A}\mathbf{c} = \mathbf{b}, \quad (11)$$

where $\mathbf{A} = (\mathbf{D}_{of}\mathbf{B}_{of})^T (\mathbf{D}_{of}\mathbf{B}_{of}) + \lambda_d \mathbf{B}_d^T \mathbf{B}_d + \lambda_s \mathbf{B}_s^T \mathbf{B}_s$, and $\mathbf{b} = (\mathbf{D}_{of}\mathbf{B}_{of})^T \mathbf{I}_{of,t}$. \mathbf{A} is a matrix with size $2M_t N_t \times 2M_t N_t$ and \mathbf{b} is a column vector with size $2M_t N_t \times 1$.

Since a truncated discrete cosine basis was used, the size of \mathbf{A} was significantly reduced from $2MN \times 2MN$ to $2M_t N_t \times 2M_t N_t$. The small size allows to derive a solution to Eq. (11) using direct methods instead of iterative methods, such as the successive over-relaxation method used in [17]. Mathematically, there is a unique solution when matrix \mathbf{A} is full-rank. In practice, \mathbf{A} could be rank-deficient or ill-conditioned due to noisy measurements. In our implementation, the addition of small values from matrices $\mathbf{B}_d^T \mathbf{B}_d$ and $\mathbf{B}_s^T \mathbf{B}_s$, which are regulated with λ_d and λ_s , into the elements of the matrix $(\mathbf{D}_{of}\mathbf{B}_{of})^T (\mathbf{D}_{of}\mathbf{B}_{of})$ helped to avoid the ill-posed or ill-conditioned problem. In this study, we used the Matlab function “mldivide.m” to solve Eq. (11). It returns an exact solution when \mathbf{A} is full-rank and a least squares solution when \mathbf{A} is rank-deficient.

In addition, above least squares estimation on a motion field is usually sensitive to outliers, which are associated with violation of the optical flow constraint given by Eq. (1). To avoid it, a weighted least squares was performed to assign low weights

to outliers after the first least squares estimation. The weights were expressed as $\mathbf{w} = \frac{1}{1+R}$, where $R = |I_x U_x + I_y U_y + I_t|$ is the absolute value of residuals of the optical flow equation to evaluate the estimation bias of each sample. Applying weights on each sample, the final estimation of DCT coefficients $\hat{\mathbf{c}}$ was solved as:

$$\hat{\mathbf{c}} = \left(\hat{\mathbf{A}}^T \hat{\mathbf{A}} \right)^{-1} \hat{\mathbf{A}}^T \hat{\mathbf{b}}, \quad (12)$$

where $\hat{\mathbf{A}} = (\mathbf{D}_{of} \mathbf{B}_{of})^T \mathbf{W} (\mathbf{D}_{of} \mathbf{B}_{of}) + \lambda_d \mathbf{B}_d^T \mathbf{B}_d + \lambda_s \mathbf{B}_s^T \mathbf{B}_s$, $\hat{\mathbf{b}} = (\mathbf{D}_{of} \mathbf{B}_{of})^T \mathbf{W} \mathbf{b}$ and \mathbf{W} is a weight matrix with size $MN \times MN$, whose column elements are \mathbf{w} .

C. Algorithm Implementation

The proposed algorithm consisted of 7 steps:

- Step 1: Segment manually the vascular wall on a middle frame of an RF image sequence to generate a ROI. The ROI on remaining frames was propagated using an automatic segmentation algorithm [42] that allowed tracking translation motion and small changes in ROI boundary at given frames.
- Step 2: Normalize the RF image sequence with the maximum value of image intensities.
- Step 3: Choose pixels inside the ROI generated in Step 1 to do calculation.
- Step 4: Build vectors and matrices in Eq. (11) using Eqs (7), (8), and (9), and solve the least squares system of Eq. (11) to obtain DCT coefficients \mathbf{c} .
- Step 5: Introduce DCT coefficients \mathbf{c} estimated in Step 4 into Eq. (4) to compute displacement fields.
- Step 6: Compute \mathbf{W} with the displacement field from the previous step. With computed weights \mathbf{W} , solve DCT coefficients $\hat{\mathbf{c}}$ using Eq. (12).
- Step 7: Introduce DCT coefficients $\hat{\mathbf{c}}$ into Eq. (5) to compute principal strain components using Eq. (6).

III. SIMULATIONS AND EXPERIMENTS

A. Simulations

A carotid artery model was created using COMSOL Multiphysics (Structural Mechanics Module, version 3.5, COMSOL, France) whose geometry was described in [43]. A soft necrotic core (elasticity modulus $E = 10$ kPa) and four calcified inclusions ($E = 5000$ kPa) were embedded in a medium ($E = 600$ kPa) mimicking a fibrous plaque. All plaque components were considered nearly incompressible (Poisson' ratio = 0.4995). To avoid rigid motions of the model, a soft ($E = 1$ Pa) and compressible layer (Poisson's ratio = 0.001) of 1 mm thickness was added on the outer layer. This artificial outer contour was anchored and was not considered in the strain analysis. The density of randomly distributed scatterers included in the vascular model was 100 per resolution cell to ensure fully developed speckle [44]. In this study, the resolution cell volume was defined as a cubic whose size in each direction (axial, lateral and elevation) is one wavelength of the transmitted pulse [45]–[47]. The wavelength is about 0.2 mm for a 7.2 MHz central frequency transducer.

A systemic blood pressure waveform with pressure changes from 80 to 120 mmHg (10 to 16 kPa) was applied to the simulated model. The pressure waveform was divided into

500 segments to allow mimicking a frame rate of 500 s⁻¹. For each intraluminal pressure difference, displacements and strains of the vessel wall were calculated using a finite elements method (FEM) under plane strain condition. These displacements plus pre-deformation positions were used to update the post-deformation positions of scatterers. The strains were used as gold standard for comparison.

Cross-sectional RF data were simulated using the ultrasound simulation program Field II [48]. A L14-5/38 linear array probe with 128 elements (Ultrasonix Medical Corporation, Richmond, BC, Canada) was simulated with a 7.2 MHz center frequency and a 40 MHz sampling rate. The full aperture was considered as activated in transmission to create plane waves with emission angles ranging from -10° to 10° with 1° increment. Plane wave data with 21 angles at each intraluminal pressure difference were beamformed to create one coherent plane wave compounded (CPWC) image using a delay-and-sum algorithm [49]. All beamformed images were corrupted with white Gaussian noise to make them more realistic with signal-to-noise ratios (SNR) of 20 dB. To evaluate the robust against global noise, additional 5 dB, 10 dB, 15 dB, and 25 dB SNR images were generated by adding white Gaussian noise globally. To evaluate the robustness of strain estimation algorithms against localized noise, the 20 dB SNR images were corrupted with additional white Gaussian noise at four specific regions where SNR was reduced to 5 dB. The four regions were evenly divided into the upper left, upper right, lower left and lower right regions by considering the image center (see Fig. 3).

B. In Vitro Experiments

In vitro data from two vascular phantoms, one homogeneous and the other heterogeneous, were used to validate the proposed SMSE algorithm. These phantoms were made of 10% polyvinyl alcohol mixed with 3% acoustic scatterers (Sigmacell cellulose, type 50, Sigma Chemical, St Louis, MO, USA). To fabricate the homogeneous phantom, two molds, a hollow cylindrical mold and a solid stem, were designed and generated using a 3-D printer (Dimension Elite, Stratasys Inc., Eden Prairie, MN, USA). Then, polyvinyl alcohol materials were poured between the two molds. The homogeneous phantom was solidified using 6 freeze-thaw cycles to obtain a modulus of 182 ± 21 kPa [50]. The heterogeneous phantom consisted in a soft inclusion within a vascular wall mimicking a lipid plaque. To fabricate it, a solid stem mold with the cross sectional shape of a soft inclusion was printed. After assembling previous outer and inner molds with the soft inclusion mold, polyvinyl alcohol materials were poured and underwent 5 freeze-thaw cycles. Then, the soft inclusion mold was removed and a second injection of polyvinyl alcohol materials was introduced into the hole left by the soft inclusion mold. The whole phantom then underwent a last freeze-thaw cycle. The soft inclusion thus experienced 1 freeze-thaw cycle giving a modulus of 25 ± 3 kPa [50]; whereas the surrounding vascular wall underwent 6 freeze-thaw cycles, similar to the homogeneous phantom.

Each phantom was suspended in a water tank and pressurized by connecting the tube outlet to a water column.

The intraluminal pressure was varied from 60 mmHg to 120 mmHg with a pulsatile pump (model 1421, Harvard Apparatus, Holliston, MA, USA). The pressure was monitored using a ViVitest software system (Vivitro Labs Inc., Victoria, BC, Canada).

C. In Vivo Experiments

To further validate the proposed strain estimator, RF data of a common carotid artery were acquired from a 30 year-old healthy male. The study was approved by the human ethical review board of the Centre Hospitalier de l'Université de Montréal. The volunteer signed an informed consent.

D. Data Acquisition and Image Reconstruction

For *in vitro* and *in vivo* experiments, RF data in a cross-sectional view were acquired using a Sonix Touch ultrasonic system (Ultrasonix Medical Corporation, Richmond, BC, Canada) equipped with a L14-5/38 linear array probe with 128 elements, as considered in the simulation study. Plane wave data were generated and stored with full aperture using a Sonix DAQ multi-channel system and the development kit software (TexoSDK, v6.0.1). As for simulations, CPWC images were beamformed in post-processing using a delay-and-sum algorithm [49] and emission angles ranging from -10° to 10° with 1° increment (final frame rate of 500 s^{-1}). RF images were reconstructed on a regular Cartesian grid with $50 \times 20 \mu\text{m}$ resolution (lateral \times axial). All RF images were normalized in intensity before performing elastography computations.

E. Parameter Selections

In Eq. (3), λ_s and λ_d govern the influence of smoothness and nearly incompressibility constraints. Different pairs of these two parameters were tested using simulation data with a SNR of 20 dB (see results in supplementary materials, Fig. S2). The test ranges for λ_s and λ_d were both from 0.01 to 1 with an increment of 0.01. The smoothness and nearly incompressibility constraints were assumed to have the same influence on simulated, *in vitro* and *in vivo* strain estimates. Thus, the parameter pair providing the least estimation error was chosen for all reported results. The same regularization parameters $\lambda_s = 0.05$ and $\lambda_d = 0.6$ were used for all analyses, which prevented fine tuning the results and allowed a common framework for all datasets.

The property of energy compaction of DCT coefficients encourages representing the motion field with a limited number of coefficients. In this study, we choose to truncate DCT coefficients with sizes M_t and N_t in the low frequency domain. The truncation allowed reducing the equation number in Eq. (11) from $2MN$ to $2M_tN_t$, which impacted positively

the computational complexity compared with a reconstruction with all DCT coefficients. Another advantage of the truncation is the lower number of equations that allows to derive an analytical solution efficiently without an iterative process. Furthermore, the truncation ignores DCT coefficients at higher frequencies. Consequently, since motion fields are expected to be spatially smooth, this low pass filtering also improved the accuracy of elastograms.

In addition, the effect of the smoothness term in the cost function is alleviated (λ_s is smaller than λ_d) as the reconstruction with truncated DCT coefficients already eliminates high frequency noise. For a sparse representation of Eq. (3), sizes of the truncated discrete cosine basis M_t and N_t were chosen to reconstruct motion fields based on prior information. To our knowledge, there is no guideline on DCT numbers to reconstruct a motion field. Here, we propose using a cut-off frequency, $k_{cut-off}$, to determine M_t and N_t . Cut-off values were computed as M_t or $N_t = k_{cut-off}/k_{max} \times M$ (or N), where $k_{max} = 1/(2 \times \text{lateral grid resolution for } M \text{ or axial grid resolution for } N)$ is the maximum frequency in the DCT domain. Since, the thickness of the carotid artery wall with a plaque can be assumed smaller than 3 mm [51], we limited the minimum wavelength of the cosine basis function to 1.5 mm. Thus, the truncated number of DCT coefficients, M_t or N_t , was given by the Cartesian grid resolution (lateral or axial) / 1.5 mm \times image size (lateral M or axial N).

F. Criteria for Evaluation

1) *Comparison With the Lagrangian Speckle Model Estimator (LSME)*: The LSME estimator of [6] was applied to simulation, *in vitro* and *in vivo* data to compare with the proposed algorithm. The LSME is a window-based strain estimator. In each window, tissue motion is defined as an affine transformation model that is applied into the optical flow constraint equation. Specifically, the displacement of an arbitrary pixel can be described by an affine representation using its 1st order Taylor expansion. Thus, the optical flow constraint equation (Eq. (1)) can be written as $I_x (U_x + xS_{xx} + yS_{xy}) + I_y (U_y + xS_{yx} + yS_{yy}) = -I_t$.

Although a full incompressibility assumption (*i.e.*, $S_{xx} = -S_{yy}$) is considered, there are still five unknown variables in this equation. The LSME assumes that the affine motion field of pixels within a measurement window with $p \times q$ pixels is the same allowing to build an over-determined linear equation system given by Eq. (13).

The affine motion field of the centroid of the measurement window is solved using a least squares method. In the framework of high frame rate CPWC imaging, the small time step between consecutive frames allows further processing. Instead of using a pair of consecutive frames for strain

$$\begin{bmatrix} I_{x_1 y_1} & I_{x_1} & I_{y_1 x_1} & I_{y_1 y_1} - I_{x_1 x_1} & I_{y_1} \\ \vdots & \vdots & \vdots & \vdots & \vdots \\ I_{x_{p \times q} y_{p \times q}} & I_{x_{p \times q}} & I_{y_{p \times q} x_{p \times q}} & I_{y_{p \times q} y_{p \times q}} - I_{x_{p \times q} x_{p \times q}} & I_{y_{p \times q}} \end{bmatrix} \cdot \begin{bmatrix} S_{xy} \\ U_x \\ S_{yx} \\ S_{yy} \\ U_y \end{bmatrix} = - \begin{bmatrix} I_t \\ \vdots \\ I_{t_{p \times q}} \end{bmatrix}. \quad (13)$$

estimation, as in the original proposal of the method [52], a time-ensemble strategy was considered in [6]. Assuming motions of successive n_t frame pairs over a given time duration are the same, the number of equations in Eq. (13) is increased n_t times, which allows increasing the robustness of the least squares estimation problem. For a fair comparison, the estimation parameters were the same as in [10]. Namely, the window size was set to 1.0 mm \times 1.0 mm with 80% overlap in axial and lateral directions, and the time-ensemble number n_t was 8 with 90% time overlap.

2) Evaluation of Strain Estimation Performance: For simulated data, an image sequence of one pressure cycle was selected and all 2-D strain components (S_{xx} , S_{xy} , S_{yy} , S_{yx}) were computed over consecutive frames and cumulated. Principal strains were determined using Eq. (6) and the largest cumulated strain map was considered as the final elastogram. Since reference strain values are known for simulations, the normalized root-mean-square-error (NRMSE) was used to evaluate elastograms in that case:

$$NRMSE = \frac{\sqrt{\frac{\sum_{i=1}^N (ref_i - est_i)^2}{N}}}{ref_{max} - ref_{min}}, \quad (14)$$

where N is the number of pixels in an elastogram, ref is the ground truth principal strain from the finite elements analysis, and est is the estimated principal strains. The subscripts max and min refer to the maximum and minimum values of the principal strain map.

The metric for evaluation of cumulated strains of *in vitro* and *in vivo* studies was the residual strain. The rationale is that the carotid artery should restore its initial state after an entire cycle. The residual strain is a good indicator to evaluate cumulative estimation errors in vascular elastography [53], [54]. The less residual strain means less cumulative estimation errors. In this study, a whole cycle was determined by two periodic zero-crossing points on the time-varying principal strain curve. The residual strain was calculated as the mean strain value of the cumulated end frame for a full cardiac cycle. In addition to the residual strain metric, the reproducibility of cumulative strain curves was evaluated for *in vivo* results. Two successive cardiac cycles of cumulated principal strain maps were estimated and spatially averaged to obtain mean principal strain curves. Unlike computing a correlation coefficient of two strain curves, as done in [55], we performed a linear regression of the two strain curves to fit a function, $y = ax + b$, where x , y are strain curves of two successive cycles, and a , b are fitted coefficients. Here, a was used to evaluate the similarity between the two consecutive cyclic strain curves, and it was expected to be 1 when the two curves are the same. The intercept b was used to evaluate residual strain errors, and in this case it was expected to be 0 when there is no residual strain error.

3) Other Assessments of Strain Estimation Algorithms: Additionally, computation time for a whole image sequence was viewed as an indicator of algorithm efficiency. To assess this, the LSME and proposed SMSE algorithms were both implemented in Matlab 2016a (MathWorks Inc., Natick, MA, USA) on a 4-core CPU at 3.7 GHz.

Finally, additional *in vitro* measurements were performed to compare the strain image resolution of both LSME and SMSE algorithms. Two soft phantoms with hard inclusions were fabricated. The first one had three hard inclusions of 2 mm, 1 mm and 0.8 mm at the same depth. The other was made with three hard inclusions of 2 mm but at different depths. The soft background was made with 0.3% agar (A9799, Sigma-Aldrich Chemical, St Louis, MO), 4% gelatin (G2500, Sigma-Aldrich Chemical), 8% glycerol, and 87.7% distilled water. Hard inclusions were fabricated with 15% polyvinyl alcohol, 3% cellulose particles (Sigmacell, type 5504, Sigma Chemical), and 82% distilled water that underwent 6 freeze-thaw cycles.

Since cross sectional sizes of hard inclusions are small, they could not be fabricated by simply pouring polyvinyl alcohol materials into a mold. Thus, we used a syringe to inject the solution into cylindrical tubes with inner diameters of 2 to 0.8 mm. After 6 freeze-thaw cycles, the cylindrical polyvinyl alcohol materials were extracted from the tubes to mimic hard inclusions. Then, the ends of cylindrical hard inclusions were horizontally fastened on the walls of a cubic plastic box. The soft mixture of agar, gelatin, glycerol and distilled water was poured into the mold. After cooling down the mixture to room temperature, the phantom was made by removing the plastic box. Axial compressions with maximum deformations of 1 mm were launched on the top of the phantom with the ultrasound probe that was driven by a mini-shaker vibrating as a 1.2 Hz sinusoid. For the first phantom, the LSME with the same window size (1 mm \times 1 mm) but different overlaps of 50%, 80% and 95% were used to compare axial strains S_{yy} with those obtained with the proposed SMSE algorithm. For the second phantom, the LSME still had a window size of 1 mm \times 1 mm with a 80% overlap.

IV. RESULTS

A. The Simulation Study

Figure 1(a) shows a B-mode image with a SNR of 20 dB of the carotid artery simulation using CPWC imaging. Accumulated principal strain maps estimated with the LSME and SMSE are presented in Fig. 1(d)-(g). For principal minor strains, both LSME and SMSE provided similar estimation performance with NRMSE of 8.45% and 6.75% with respect to the ground true, respectively. The LSME strain map (Fig. 1(d)) allowed identifying the small hard inclusion close to the lumen at 7 o'clock, but provided less evidence of the presence of the two hard inclusions in the upper right of the model than with the SMSE (Fig. 1(f)). The estimation error of principal minor strains was reduced by 20% with the SMSE compared with the LSME. For principal major strains, the SMSE strain map (Fig. 1(g)) revealed hard inclusions better than with the LSME (Fig. 1(e)). The NRMSE in Fig. 1(e) and (g) are 9.56% and 7.02%, respectively. The estimation error of principal major strains was reduced by 27% using the SMSE. The impact of the LSME window size on strain estimates can be visualized in the zoomed ROI. The SMSE principal minor strain shows smoother inner and outer artery edges compared with the window-based LSME algorithm. A similar conclusion applies

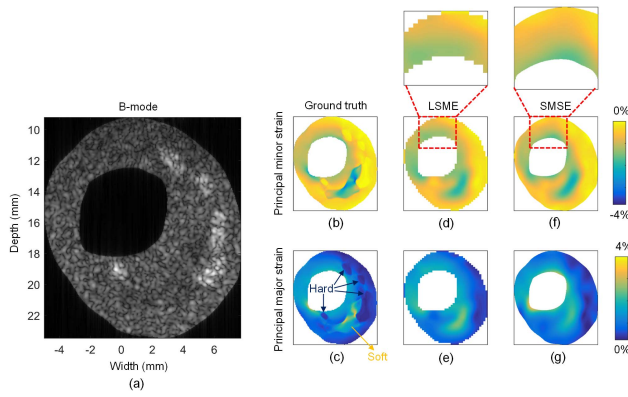


Fig. 1. (a) B-mode image of an artery simulation model with one soft inclusion and four hard inclusions. The image SNR is 20 dB. (b), (c) Principal minor and major strains of the finite-elements model ground truth. (d), (e) Accumulated principal minor and major strains using LSME, whose NRMSE are 8.45% and 9.56%, respectively. (f), (g) Accumulated principal minor and major strains using SMSE, whose NRMSE are 6.75% and 7.02%, respectively. Close-ups in the red rectangular regions are displayed to present the resolution of strain maps.

to the principal major strain map. For these results, values of M_t and N_t were 11 and 10, respectively.

To test the robustness against global noise, the LSME and SMSE accumulated principal strain elastograms were computed from simulation images by considering different SNRs from 5 dB to 25 dB. Overall, the SMSE achieved less NRMSE than the LSME for both principal minor and major strains (see results in supplementary materials, Fig. S3). Accumulated principal strain examples at SNRs of 10 dB and 15 dB are presented in Fig. 2. Results for a SNR of 20 dB can be seen in Fig. 1. As presented in Fig. 2, principal strain maps with the LSME were noisier than with the SMSE when the SNR was reduced, especially in the thin wall region of the upper left part. NRMSE of LSME principal minor and major strain maps for the SNR of 10 dB are 13.90% and 16.27%, respectively, while those errors with the SMSE are 7.54% and 8.17%, respectively. Estimation errors of principal minor and major strains were reduced by 46% and 50%, respectively, using the SMSE. As shown in Fig. 2(d), at the SNR of 15 dB, the LSME estimation performance was improved with NRMSE of 9.81% and 11.33% for principal minor and major strain maps, whereas they remained similar but better with the SMSE (NRMSE of 7.30% and 7.49% for principal minor and major strain maps, respectively).

Figure 3 presents robustness of both algorithms against localized noise (simulations with a SNR of 20 dB where the SNR was reduced to 5 dB into the upper left (a), upper right (b), lower left (c) and lower right (d) regions). All LSME accumulated principal strain maps were obviously deteriorated by the addition of local noise. NRMSE of SMSE accumulated principal strain maps nearly remained the same in all regions. Moreover, NRMSE with the SMSE were less than with the LSME (see legend of Fig. 3 for values).

B. In Vitro Experiments

1) *The Homogeneous Vascular Phantom Study:* Figure 4(a) presents a CPWC B-mode image of the homogeneous

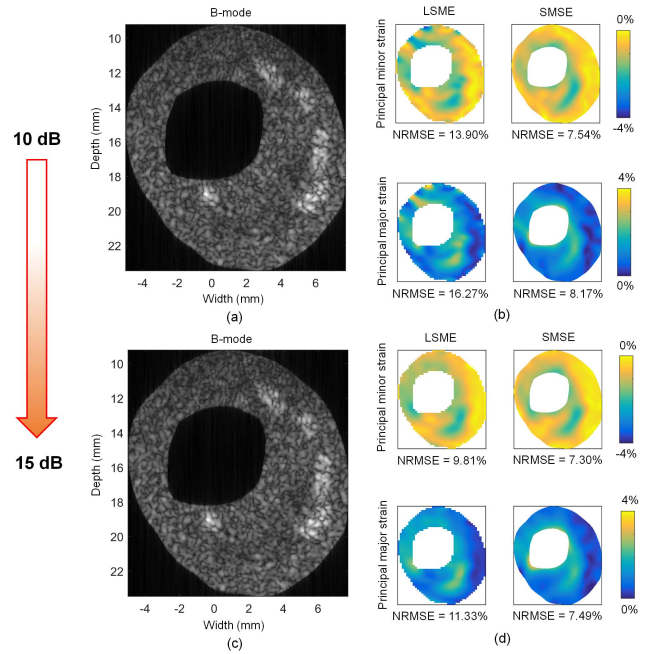


Fig. 2. (a), (b) B-mode images with a SNR of 10 dB and corresponding accumulated principal strain maps. (c), (d) B-mode images with a SNR of 15 dB and corresponding accumulated principal strain maps. NRMSEs of accumulated principal strain maps with the LSME and SMSE are shown.

vascular phantom. Figure 4(b)-(e) shows accumulated principal strain maps using the LSME and SMSE. Like simulation results, the vascular geometry was more smoothly delineated in principal strains using the SMSE (panels (d) and (e)) than with the LSME (panels (b) and (c)). According to previous literature [56], the strain magnitude is expected to decrease with increasing radial distance from the lumen, which is known as the strain decay phenomenon. Qualitatively, the strain decay is more distinct on SMSE principal strain maps. Some artifacts are noticed on LSME elastograms at the lower left region (Fig. 4(b) and (c)). Residual principal minor and major strains at the end of the flow cycle were -0.49% and 0.49% for the LSME, and they were reduced to -0.14% and 0.13% for the SMSE. Selected values of M_t and N_t for those results were 9 and 8, respectively.

2) *The Heterogeneous Phantom Study:* Figure 5 presents a CPWC B-mode image of the heterogeneous vascular phantom with a soft inclusion, and accumulated principal strains using the LSME and SMSE. The soft inclusion is identifiable on all strain maps. The strain decay phenomenon caused an overestimation of the dimension of the soft inclusion with both algorithms. Residual principal minor and major strains were -0.56% and 0.56% for the LSME, respectively. They were lower at -0.19% and 0.17% for the SMSE, respectively. Selected values of M_t and N_t were 9 and 8, respectively.

C. In Vivo Validation

Figure 6 displays an *in vivo* B-mode image of a common carotid artery. LSME and SMSE accumulated principal strain

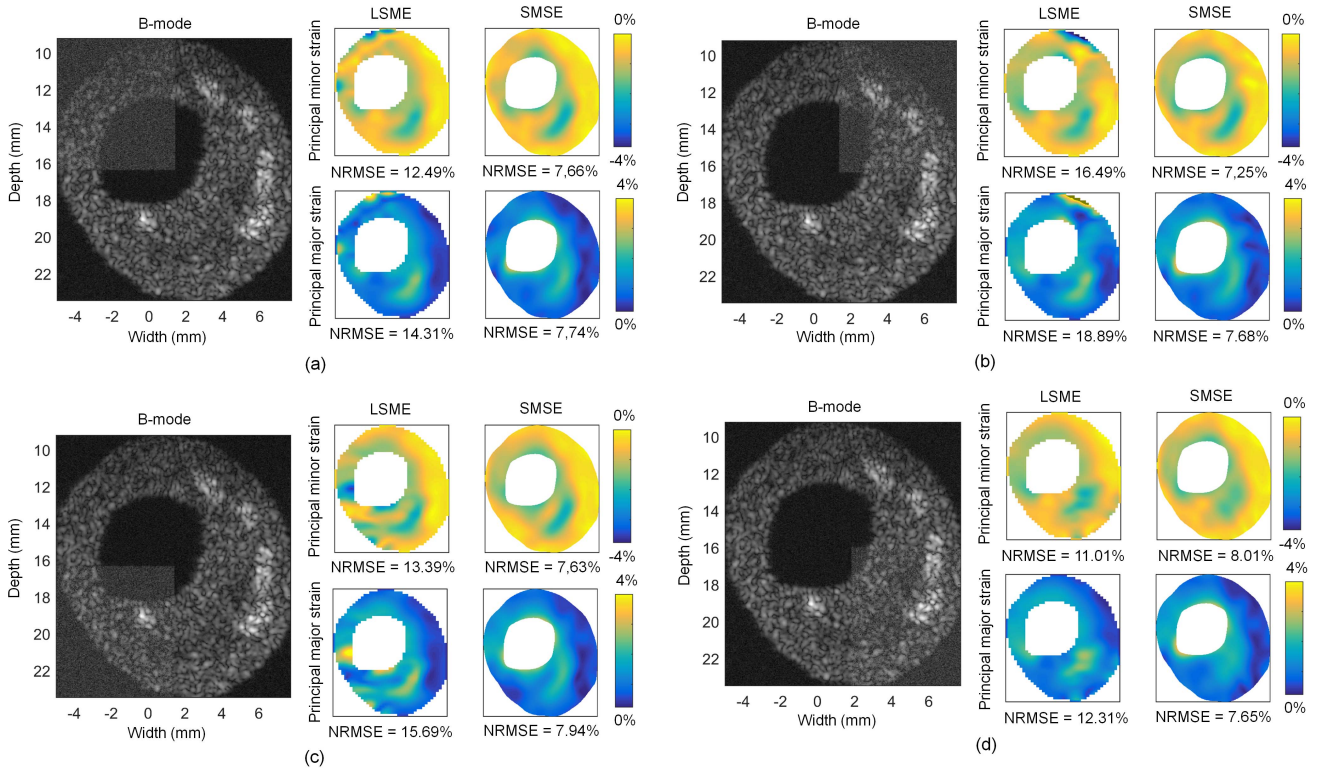


Fig. 3. B-mode images with a global SNR of 20 dB and local noise at a SNR of 5 dB in the upper left (a), upper right (b), lower left (c) and lower right (d) regions and corresponding accumulated principal strain maps. NRMSEs of accumulated principal strain maps with the LSME and SMSE are shown.

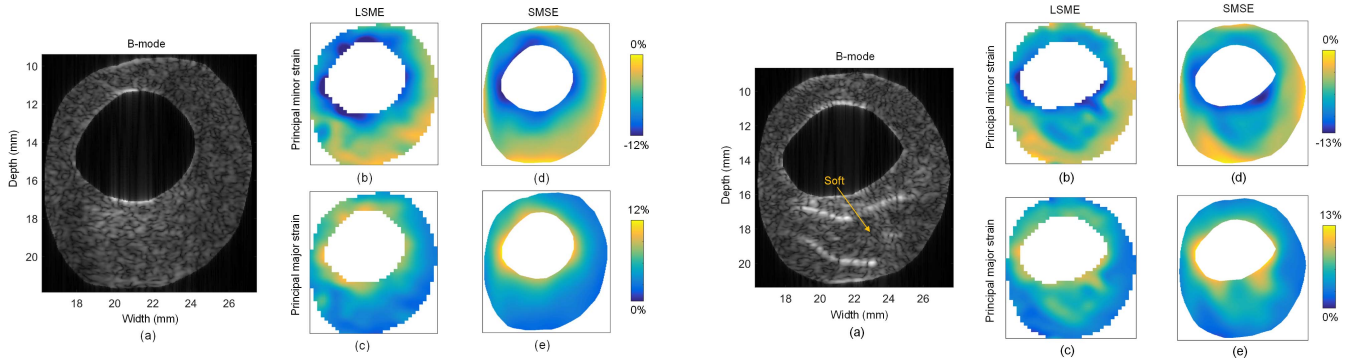


Fig. 4. (a) B-mode image of a homogeneous vascular phantom. (b), (c) Accumulated principal minor and major strains using the LSME, whose residual strains are -0.49% and 0.49% , respectively. (d), (e) Accumulated principal minor and major strains using the SMSE, whose residual strains are -0.14% and 0.13% , respectively.

Fig. 5. (a) B-mode image of a heterogeneous vascular phantom with a soft inclusion under the lumen. (b), (c) Accumulated principal minor and major strains using the LSME, whose residual strains are -0.56% and 0.56% , respectively. (d), (e) Accumulated principal minor and major strains using the SMSE, whose residual strains are -0.19% and 0.17% , respectively.

maps are shown in Fig. 6(b)-(e). Because of boundary conditions imposed by surrounding tissues, non-homogeneous strain maps are noticed with both algorithms as a function of the angular position. However, regional differences are observed when comparing both elastography methods. Residual strains at the end of the sequence for principal minor and major strain maps using the LSME were -5.56% and 5.56% , respectively, whereas they were below at -1.92% and 1.77% for the SMSE, respectively. Values of M_t and N_t were 8 and 7, respectively.

All cumulated principal strain maps over two consecutive cycles were spatially averaged. Mean strain curves for the LSME and SMSE are presented in Fig. 7. Values of end points

of mean strain curves were considered as residual strains. As quantified above, the SMSE gave less residual strain errors: 3.65% and 3.34% for principal minor and major strains, respectively, compared with -7.89% and 7.89% , respectively, in the case of the LSME. To quantify the reproducibility, strain curves of two cardiac cycles were used to perform a linear fit. As shown in Fig. 8, a higher regression coefficient a and a lower intercept b were obtained with the SMSE.

D. Computation Efficiency

Computation time for processing a whole image sequence was calculated and normalized by the number of frames

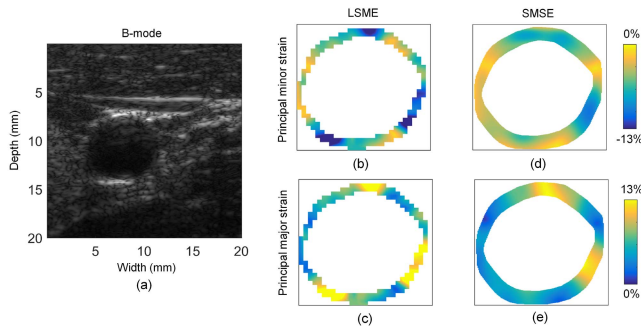


Fig. 6. (a) In vivo B-mode image of a carotid artery of a 30 year-old healthy male. (b), (c) Accumulated principal minor and major strains using the LSME, whose residual strains are -5.56% and 5.56% , respectively. (d), (e) Accumulated principal minor and major strains using the SMSE, whose residual strains are -1.92% and 1.77% , respectively.

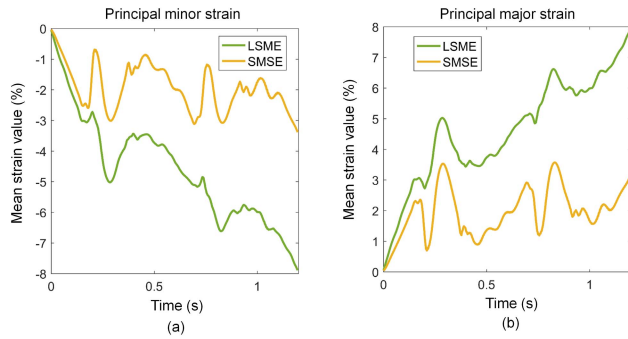


Fig. 7. (a) Mean strain curves over two consecutive cardiac cycles obtained by averaging spatially accumulated principal minor strains. Residual strains of the LSME and SMSE are -7.89% and -3.65% , respectively. (b) Mean strain curves over two consecutive cardiac cycles obtained by averaging spatially accumulated principal major strains. Residual strains of the LSME and SMSE are 7.89% and 3.34% , respectively.

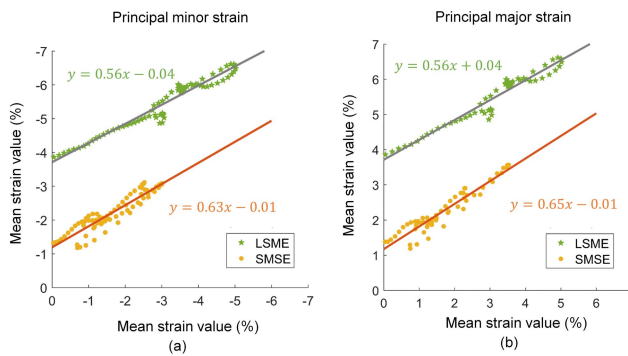


Fig. 8. Accumulated principal strain curves from the two successive cardiac cycles of Fig. 7 were selected to perform linear regressions for (a) principal minor strains of the LSME and SMSE, and (b) principal major strains of the LSME and SMSE.

per sequence. As presented in Table I, the computation time of the SMSE was reduced by 4 to 25 folds compared with the LSME regarding simulation, *in vitro* and *in vivo* data.

E. Spatial Resolution

As seen in Fig. 9, the LSME elastogram with a 50% overlap (panel b) presents a smoother strain distribution than with higher overlaps, but fails to detect the inclusion of 0.8 mm. At 80% or 95% overlap (panels c and d), the spatial sampling is improved but at the cost of a higher variance. The SMSE

TABLE I
COMPUTATION EFFICIENCY (SECOND/FRAME)

Type of experiments	LSME	SMSE
Simulations	13.1	3.0
<i>In vitro</i> - homogeneous	9.2	1.7
<i>In vitro</i> - heterogeneous	9.6	2.1
<i>In vivo</i>	7.5	0.3

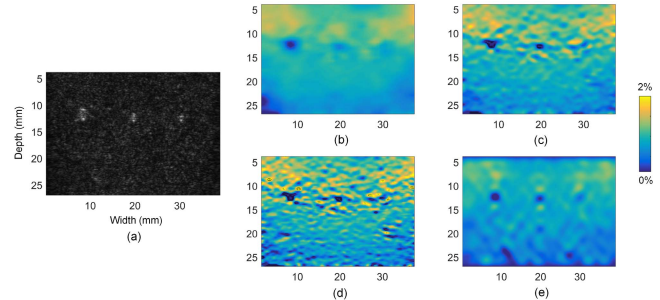


Fig. 9. (a) B-mode image of a soft phantom with three sizes of hard inclusions of 2 mm, 1 mm and 0.8 mm. (b), (c), (d) Accumulated axial strains using the LSME with a $1.0\text{ mm} \times 1.0\text{ mm}$ window size and 50%, 80% and 95% overlaps, respectively. (e) Accumulated axial strains using the SMSE.

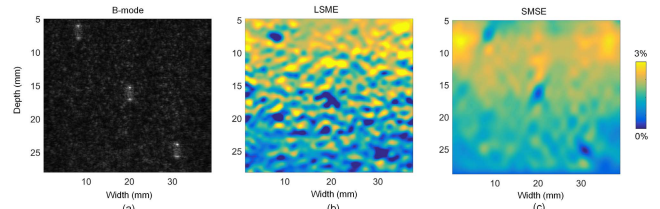


Fig. 10. (a) B-mode image of a soft phantom with three hard inclusions of 2 mm at different depths. (b) Accumulated axial strains using the LSME with a $1.0\text{ mm} \times 1.0\text{ mm}$ window size and 80% overlap. (c) Accumulated axial strains using the SMSE.

algorithm provided better results and allowed identifying all inclusion sizes. The impact of the hard inclusion depth is presented in Fig. 10 (for the 2 mm diameter inclusion). Again, the best results are obtained with the SMSE method.

V. DISCUSSION

Although dense OF estimation is already applied into computer vision [22] and myocardial motion tracking [21] to obtain displacement fields, these models required new developments for strain imaging in the context of vascular mechanical characterization. In the current study, we extended the dense OF model with DCT descriptions to derive four strain components (axial and lateral strains and shears). Those strain components were combined to obtain coordinate-system independent principal strains. Moreover, a framework with sparse representation was analytically implemented to reduce the estimation time compared with window-based strategies.

For *in vivo* results, principal strain maps were not homogeneous circumferentially (Fig. 6(b)-(e)). The same heterogeneous observation in strain maps for healthy carotid arteries were recently reported [57], [58]. The potential explanation is likely the presence of different boundary conditions surrounding the carotid artery [6]. Thus, we proposed to use a linear regression strategy to evaluate the

reproducibility of cumulated principal strain curves instead of SNR measurements, as done in [57], [58].

There is a trade-off between elastogram spatial sampling and computation efficiency for window-based approaches. The spatial sampling is determined by the window overlap, as demonstrated in Fig. 9 for the case of the LSME algorithm. Compared with the 80% window overlap used to obtain most results, the computation time was reduced 4 times when using the 50% overlap, and it was increased 46 times for the 95% overlap. The proposed SMSE method could circumvent this trade-off issue by considering all pixels globally. Even with a theoretical pixel resolution, the SMSE computation time was still lower than that of the LSME with a lower resolution. Moreover, an arbitrary resolution can be set in this SMSE implementation, which could reduce the computation time proportionally. According to *in vivo* SMSE performance whose frame rate was around 3 s^{-1} with described computer facilities and software, it is believed that real-time estimation could be achieved by combining appropriate down-sampling estimation and parallel computing.

Another trade-off of window-based approaches is the compromise between elastogram spatial sampling and artifacts. Intuitively, larger overlap can increase elastogram spatial sampling, but at an expense of increasing artifacts. As seen in Fig. 9, the axial elastogram using the LSME with a 50% overlap presented a smooth strain distribution due to a lower spatial sampling, while it failed to detect the inclusion of 0.8 mm. With an overlap of 80% or 95%, the elastogram spatial sampling was increased and it was visually possible to barely see the 0.8 mm inclusion, but at the expense of strong background variance. Moreover, worm artifacts due to a large overlap were noticed. Worm artifacts appear as thin and short alternate bands attributed to correlation noise patterns when the overlap is increased [11]. The elastogram using the SMSE avoided these artifacts and presented clear outlines of each inclusions.

In this study, we integrated a nearly incompressibility constraint into the SMSE. Also, weights were assigned into Eq. (12) to refine the solution. To evaluate the separate influence of these propositions on principal strain results, we performed additional experiments using the SMSE without the nearly incompressibility constraint or without any weights. Results can be seen in supplementary materials (Figs S4-S7). The nearly incompressibility constraint improved principal strain estimations to a large extent. However, the impact of adding weights into Eq. (12) was less significant; it mainly allowed fine tuning the solution.

It was mentioned earlier that the computation time of the SMSE is proportional to the number of equations, namely $2M_t N_t$ in Eq. (11). Additional computations were performed to illustrate this. Namely, the impact of doubling the number of DCT coefficients is presented in Table S1 of supplementary materials.

In this study, plane wave imaging was implemented to achieve a frame rate of 500 s^{-1} , which kept inter-frame motions small. However, the performance of optical flow-based methods, such as the LSME and SMSE, could be affected by large inter-frame motions that could be observed

with conventional focused ultrasound imaging. To verify this, the *in vitro* and *in vivo* data were down sampled by a factor of 10 to simulate a conventional focused ultrasound imaging frame rate of 50 s^{-1} . We found that the larger inter-frame deformations at 50 s^{-1} indeed induced larger estimation errors (about two-time larger residual strain magnitudes). Nevertheless, principal strain maps at 50 s^{-1} (see Figs S8 to S10 in supplementary materials) were similar to those at a frame rate of 500 s^{-1} (Figs 4 to 6). Since this paper is focusing on vascular elastography where vessel deformation is much less than cardiac strain or other larger deformation conditions, the proposed method is adequate and accurate in this context. To handle larger inter-frame motions, a multi-scale strategy adapted to optical flow methods would be useful.

Although the SMSE is more robust than the LSME against local noise with a SNR of 5 dB (Fig. 3) and global noise with different SNRs (Fig. 2 and Fig. S3 in supplementary materials), the performance of the SMSE when a large local region is corrupted with more noise deserves additional attention. Therefore, an additional simulation test reported in Fig. S11 of supplementary materials verified this potential issue. We found that local noise with a SNR of 1 dB instead of 5 dB simply affected local estimations of the SMSE, not global estimations over the whole artery. This implies that the SMSE is robust against localized noise and that the whole principal strain estimation process is not affected.

Theoretically, other sophisticated regularization terms that are used in dense optical flow techniques, such as sparsity of optical flow gradients [25] and non-local terms [59], [60] can be added into the proposed SMSE model as a prior knowledge instead of the nearly incompressibility term to solve the strain field. The impact of using different regularization terms on strain estimations deserves to be investigated in future studies.

Finally, the SMSE is not only able to provide robust strain estimates at a sub-mm spatial resolution, but also the assessment of the 2-D displacement field, as described by Eq. (4). Thus, the SMSE may be applicable in the context of shear wave elastography to track the 2-D velocity field [61]. Future experiments in that direction are worthy to be investigated. Beside ultrasound vascular elastography, it is believed that the proposed algorithm can also be of value for magnetic resonance elastography [62] or non-rigid object tracking in computer vision applications [63]. As shown in Fig. 10(c), the detection of small hard inclusions at different depths might also enhance the capability of current quasi-static breast compression elastography technologies [64].

VI. CONCLUSION

In this study, an affine model-based estimator including a sparsity strategy has been proposed to provide vascular strain estimations at high spatial resolution and with computational efficiency close to real-time. With simulation data, the SMSE gave less estimation errors than with the window-based LSME approach. For *in vitro* results, elastograms with the SMSE showed less residual strain errors than with the LSME. For *in vivo* results, the SMSE provided also less residual strain errors and more reproducible cumulative strain curves. Computation time was reduced significantly with the SMSE compared with

the LSME. In addition, the SMSE avoided window effects of window-based approaches.

REFERENCES

- [1] R. J. Dempsey *et al.*, "Carotid atherosclerotic plaque instability and cognition determined by ultrasound-measured plaque strain in asymptomatic patients with significant stenosis," *J. Neurosurgery*, vol. 128, no. 1, pp. 111–119, Jan. 2018.
- [2] R. L. Maurice, M. Daronat, J. Ohayon, É. Stoyanova, F. S. Foster, and G. Cloutier, "Non-invasive high-frequency vascular ultrasound elastography," *Phys. Med. Biol.*, vol. 50, no. 7, pp. 1611–1628, Apr. 2005.
- [3] H. H. G. Hansen, R. G. P. Lopata, T. Idzenga, and C. L. de Korte, "Full 2D displacement vector and strain tensor estimation for superficial tissue using beam-steered ultrasound imaging," *Phys. Med. Biol.*, vol. 55, no. 11, pp. 3201–3218, Jun. 2010.
- [4] S. Korukonda and M. Doyley, "Visualizing the radial and circumferential strain distribution within vessel phantoms using synthetic-aperture ultrasound elastography," *IEEE Trans. Ultrason., Ferroelectr., Freq. Control*, vol. 59, no. 8, pp. 1639–1653, Aug. 2012.
- [5] M. Larsson, B. Heyde, F. Kremer, L.-Å. Brodin, and J. D'hooge, "Ultrasound speckle tracking for radial, longitudinal and circumferential strain estimation of the carotid artery—An *in vitro* validation via sonomicrometry using clinical and high-frequency ultrasound," *Ultrasonics*, vol. 56, pp. 399–408, Feb. 2015.
- [6] J. Poree, D. Garcia, B. Chayer, J. Ohayon, and G. Cloutier, "Noninvasive vascular elastography with plane strain incompressibility assumption using ultrafast coherent compound plane wave imaging," *IEEE Trans. Med. Imag.*, vol. 34, no. 12, pp. 2618–2631, Dec. 2015.
- [7] C. Sumi, "Fine elasticity imaging utilizing the iterative RF-echo phase matching method," *IEEE Trans. Ultrason., Ferroelectr., Freq. Control*, vol. 46, no. 1, pp. 158–166, Jan. 1999.
- [8] A. Basarab, P. Gueth, H. Liebgott, and P. Delachartre, "Phase-based block matching applied to motion estimation with unconventional beam-forming strategies," *IEEE Trans. Ultrason., Ferroelectr., Freq. Control*, vol. 56, no. 5, pp. 945–957, May 2009.
- [9] M. Alessandrini *et al.*, "A new technique for the estimation of cardiac motion in echocardiography based on transverse oscillations: A preliminary evaluation in Silico and a feasibility demonstration *in vivo*," *IEEE Trans. Med. Imag.*, vol. 33, no. 5, pp. 1148–1162, May 2014.
- [10] H. Li, J. Poree, M.-H. Roy Cardinal, and G. Cloutier, "Two-dimensional affine model-based estimators for principal strain vascular ultrasound elastography with compound plane wave and transverse oscillation beamforming," *Ultrasonics*, vol. 91, pp. 77–91, Jan. 2019.
- [11] J. Ophir *et al.*, "Elastography: Ultrasonic estimation and imaging of the elastic properties of tissues," *Proc. Inst. Mech. Eng. H, J. Eng. Med.*, vol. 213, no. 3, pp. 203–233, Mar. 1999.
- [12] U. Techavipoo and T. Varghese, "Wavelet denoising of displacement estimates in elastography," *Ultrasound Med. Biol.*, vol. 30, no. 4, pp. 477–491, Apr. 2004.
- [13] E. Brusseau, J. Kybic, J.-F. Deprez, and O. Basset, "2-D locally regularized tissue strain estimation from radio-frequency ultrasound images: Theoretical developments and results on experimental data," *IEEE Trans. Med. Imag.*, vol. 27, no. 2, pp. 145–160, Feb. 2008.
- [14] H. Rivaz, E. M. Boctor, M. A. Choti, and G. D. Hager, "Real-time regularized ultrasound elastography," *IEEE Trans. Med. Imag.*, vol. 30, no. 4, pp. 45–928, Apr. 2011.
- [15] H. Rivaz, E. M. Boctor, M. A. Choti, and G. D. Hager, "Ultrasound elastography using multiple images," *Med. Image Anal.*, vol. 18, no. 2, pp. 314–329, Feb. 2014.
- [16] M. Omidyeganeh, Y. Xiao, M. O. Ahmad, and H. Rivaz, "Estimation of strain elastography from ultrasound radio-frequency data by utilizing analytic gradient of the similarity metric," *IEEE Trans. Med. Imag.*, vol. 36, no. 6, pp. 1347–1358, Jun. 2017.
- [17] H. S. Hashemi and H. Rivaz, "Global time-delay estimation in ultrasound elastography," *IEEE Trans. Ultrason., Ferroelectr., Freq. Control*, vol. 64, no. 10, pp. 1625–1636, Oct. 2017.
- [18] M. Ashikuzzaman, C. J. Gauthier, and H. Rivaz, "Global ultrasound elastography in spatial and temporal domains," *IEEE Trans. Ultrason., Ferroelectr., Freq. Control*, vol. 66, no. 5, pp. 876–887, May 2019.
- [19] M. Arigovindan, M. Suhling, C. Jansen, P. Hunziker, and M. Unser, "Full motion and flow field recovery from echo Doppler data," *IEEE Trans. Med. Imag.*, vol. 26, no. 1, pp. 31–45, Jan. 2007.
- [20] N. Ouzir, A. Basarab, B. Liebgott, B. Harbaoui, and J.-Y. Tourneret, "Motion estimation in echocardiography using sparse representation and dictionary learning," *IEEE Trans. Image Process.*, vol. 27, no. 1, pp. 64–77, Jan. 2018.
- [21] N. Ouzir, A. Basarab, O. Lairez, and J.-Y. Tourneret, "Robust optical flow estimation in cardiac ultrasound images using a sparse representation," *IEEE Trans. Med. Imag.*, vol. 38, no. 3, pp. 741–752, Mar. 2019.
- [22] B. K. P. Horn and B. G. Schunck, "Determining optical flow," *Artif. Intell.*, vol. 17, nos. 1–3, pp. 185–203, Aug. 1981.
- [23] X. Shen and Y. Wu, "Exploiting sparsity in dense optical flow," in *Proc. IEEE Int. Conf. Image Process.*, Sep. 2010, pp. 741–744.
- [24] X. Shen and Y. Wu, "Sparsity model for robust optical flow estimation at motion discontinuities," in *Proc. IEEE Comput. Soc. Conf. Comput. Vis. Pattern Recognit.*, Jun. 2010, pp. 2456–2463.
- [25] J. Han, F. Qi, and G. Shi, "Gradient sparsity for piecewise continuous optical flow estimation," in *Proc. 18th IEEE Int. Conf. Image Process.*, Sep. 2011, pp. 2389–2392.
- [26] D. L. Donoho, "Compressed sensing," *IEEE Trans. Inf. Theory*, vol. 52, no. 4, pp. 1289–1306, Apr. 2006.
- [27] F. Kallel and J. Ophir, "A least-squares strain estimator for elastography," *Ultrason. Imag.*, vol. 19, no. 3, pp. 195–208, Jul. 1997.
- [28] J. Luo, J. Bai, P. He, and K. Ying, "Axial strain calculation using a low-pass digital differentiator in ultrasound elastography," *IEEE Trans. Ultrason., Ferroelectr., Freq. Control*, vol. 51, no. 9, pp. 1119–1127, Sep. 2004.
- [29] K. Liu, P. Zhang, J. Shao, X. Zhu, Y. Zhang, and J. Bai, "A 2D strain estimator with numerical optimization method for soft-tissue elastography," *Ultrasonics*, vol. 49, no. 8, pp. 723–732, Dec. 2009.
- [30] J. Poree, M. Baudet, F. Tournoux, G. Cloutier, and D. Garcia, "A dual tissue-Doppler optical-flow method for speckle tracking echocardiography at high frame rate," *IEEE Trans. Med. Imag.*, vol. 37, no. 9, pp. 2022–2032, Sep. 2018.
- [31] T. Corpetti, E. Mémin, and P. Pérez, "Dense estimation of fluid flows," *IEEE Trans. Pattern Anal. Mach. Intell.*, vol. 24, no. 3, pp. 365–380, Mar. 2002.
- [32] L. Amodei and M. N. Benbourhim, "A vector spline approximation," *J. Approximation Theory*, vol. 67, no. 1, pp. 51–79, Oct. 1991.
- [33] S. N. Gupta and J. L. Prince, "On div-curl regularization for motion estimation in 3-D volumetric imaging," in *Proc. 3rd IEEE Int. Conf. Image Process.*, Sep. 1996, pp. 929–932.
- [34] T. Rohlfing, C. R. Maurer, D. A. Bluenken, and M. A. Jacobs, "Volume-preserving nonrigid registration of MR breast images using free-form deformation with an incompressibility constraint," *IEEE Trans. Med. Imag.*, vol. 22, no. 6, pp. 730–741, Jun. 2003.
- [35] B. Chakraborty, Z. Liu, B. Heyde, J. Luo, and J. D'hooge, "2-D myocardial deformation imaging based on RF-based nonrigid image registration," *IEEE Trans. Ultrason., Ferroelectr., Freq. Control*, vol. 65, no. 6, pp. 1037–1047, Jun. 2018.
- [36] A. Karimi, T. Sera, S. Kudo, and M. Navidbakhsh, "Experimental verification of the healthy and atherosclerotic coronary arteries incompressibility via digital image correlation," *Artery Research*, vol. 16, pp. 1–7, Dec. 2016.
- [37] T. Liang, L. Yung, and W. Yu, "On feature motion decorrelation in ultrasound speckle tracking," *IEEE Trans. Med. Imag.*, vol. 32, no. 2, pp. 435–448, Feb. 2013.
- [38] T. Mansi, X. Pennec, M. Sermesant, H. Delingette, and N. Ayache, "ILogDemons: A demons-based registration algorithm for tracking incompressible elastic biological tissues," *Int. J. Comput. Vis.*, vol. 92, no. 1, pp. 92–111, Mar. 2011.
- [39] A. Gomez, K. Pushparajah, J. M. Simpson, D. Giese, T. Schaeffter, and G. Penney, "A sensitivity analysis on 3D velocity reconstruction from multiple registered echo Doppler views," *Med. Image Anal.*, vol. 17, no. 6, pp. 616–631, Aug. 2013.
- [40] A. Gomez *et al.*, "4D blood flow reconstruction over the entire ventricle from wall motion and blood velocity derived from ultrasound data," *IEEE Trans. Med. Imag.*, vol. 34, no. 11, pp. 2298–2308, Nov. 2015.
- [41] S. A. Khayam, "The discrete cosine transform (DCT): Theory and application," *Michigan State Univ.*, vol. 114, pp. 1–31, Mar. 2003.
- [42] F. Destrempes, J. Meunier, M. F. Giroux, G. Soulez, and G. Cloutier, "Segmentation of plaques in sequences of ultrasonic B-mode images of carotid arteries based on motion estimation and a Bayesian model," *IEEE Trans. Biomed. Eng.*, vol. 58, no. 8, pp. 2202–2211, Aug. 2011.
- [43] J. Poree, B. Chayer, G. Soulez, J. Ohayon, and G. Cloutier, "Noninvasive vascular modulusology method for imaging the local elasticity of atherosclerotic plaques: Simulation and *in vitro* vessel phantom study," *IEEE Trans. Ultrason., Ferroelectr., Freq. Control*, vol. 64, no. 12, pp. 1805–1817, Dec. 2017.

- [44] R. F. Wagner, S. W. Smith, J. M. Sandrik, and H. Lopez, "Statistics of speckle in ultrasound B-scans," *IEEE Trans. Sonics Ultrason.*, vol. 30, no. 3, pp. 156–163, May 1983.
- [45] B. M. Asl and A. Mahloojifar, "Minimum variance beamforming combined with adaptive coherence weighting applied to medical ultrasound imaging," *IEEE Trans. Ultrason., Ferroelectr., Freq. Control*, vol. 56, no. 9, pp. 1923–1931, Sep. 2009.
- [46] I. K. Holfort, F. Gran, and J. A. Jensen, "Broadband minimum variance beamforming for ultrasound imaging," *IEEE Trans. Ultrason., Ferroelectr., Freq. Control*, vol. 56, no. 2, pp. 314–325, Feb. 2009.
- [47] X. Zeng, C. Chen, and Y. Wang, "Eigenspace-based minimum variance beamformer combined with Wiener postfilter for medical ultrasound imaging," *Ultrasonics*, vol. 52, no. 8, pp. 996–1004, Dec. 2012.
- [48] J. A. Jensen, "Field: A program for simulating ultrasound systems," *Med. Biol. Eng. Comput.*, vol. 34, no. 1, pp. 351–353, 1996.
- [49] G. Montaldo, M. Tanter, J. Bercoff, N. Bencech, and M. Fink, "Coherent plane-wave compounding for very high frame rate ultrasonography and transient elastography," *IEEE Trans. Ultrason., Ferroelectr., Freq. Control*, vol. 56, no. 3, pp. 489–506, Mar. 2009.
- [50] J. Fromageau, J.-L. Gennisson, C. Schmitt, R. L. Maurice, R. Mongrain, and G. Cloutier, "Estimation of polyvinyl alcohol cryogel mechanical properties with four ultrasound elastography methods and comparison with gold standard testings," *IEEE Trans. Ultrason., Ferroelectr., Freq. Control*, vol. 54, no. 3, pp. 498–509, Mar. 2007.
- [51] M. Amato *et al.*, "Carotid plaque-thickness and common carotid IMT show additive value in cardiovascular risk prediction and reclassification," *Atherosclerosis*, vol. 263, pp. 412–419, Aug. 2017.
- [52] R. L. Maurice, J. Ohayon, Y. Fretigny, M. Bertrand, G. Soulez, and G. Cloutier, "Noninvasive vascular elastography: Theoretical framework," *IEEE Trans. Med. Imag.*, vol. 23, no. 2, pp. 164–180, Feb. 2004.
- [53] H. H. G. Hansen, A. E. C. M. Saris, N. R. Vaka, M. M. Nillesen, and C. L. de Korte, "Ultrafast vascular strain compounding using plane wave transmission," *J. Biomech.*, vol. 47, no. 4, pp. 815–823, Mar. 2014.
- [54] S. Fekkes *et al.*, "2-D versus 3-D cross-correlation-based radial and circumferential strain estimation using multiplane 2-D ultrafast ultrasound in a 3-D atherosclerotic carotid artery model," *IEEE Trans. Ultrason., Ferroelectr., Freq. Control*, vol. 63, no. 10, pp. 1543–1553, Oct. 2016.
- [55] H. Li *et al.*, "Investigation of out-of-plane motion artifacts in 2D noninvasive vascular ultrasound elastography," *Phys. Med. Biol.*, vol. 63, no. 24, Dec. 2018, Art. no. 245003.
- [56] B. M. Shapo, J. R. Crowe, A. R. Skovoroda, M. J. Eberle, N. A. Cohn, and M. O'Donnell, "Displacement and strain imaging of coronary arteries with intraluminal ultrasound," *IEEE Trans. Ultrason., Ferroelectr., Freq. Control*, vol. 43, no. 2, pp. 234–246, Mar. 1996.
- [57] R. Nayak *et al.*, "Principal strain vascular elastography: Simulation and preliminary clinical evaluation," *Ultrasound Med. Biol.*, vol. 43, no. 3, pp. 682–699, Mar. 2017.
- [58] Z. Liu, Q. He, and J. Luo, "Spatial angular compounding with affine-model-based optical flow for improvement of motion estimation," *IEEE Trans. Ultrason., Ferroelectr., Freq. Control*, vol. 66, no. 4, pp. 701–716, Apr. 2019.
- [59] D. Sun, S. Roth, and M. J. Black, "Secrets of optical flow estimation and their principles," in *Proc. IEEE Comput. Soc. Conf. Comput. Vis. Pattern Recognit.*, 2010, pp. 2432–2439.
- [60] W. Dong, G. Shi, X. Hu, and Y. Ma, "Nonlocal sparse and low-rank regularization for optical flow estimation," *IEEE Trans. Image Process.*, vol. 23, no. 10, pp. 4527–4538, Oct. 2014.
- [61] M. Tanter, M. Pernot, J. L. Gennisson, and M. Fink, "A review of the medical applications of shear wave elastography," *J. Acoust. Soc. Amer.*, vol. 134, no. 5, p. 4009, 2013.
- [62] Y. K. Mariappan, K. J. Glaser, and R. L. Ehman, "Magnetic resonance elastography: A review," *Clin. Anatomy*, vol. 23, pp. 497–511, Jul. 2010.
- [63] S. Duffner and C. Garcia, "PixelTrack: A fast adaptive algorithm for tracking non-rigid objects," in *Proc. IEEE Int. Conf. Comput. Vis.*, Dec. 2013, pp. 2480–2487.
- [64] A. Itoh *et al.*, "Breast disease: Clinical application of US elastography for diagnosis," *Radiology*, vol. 239, no. 2, pp. 341–350, May 2006.